

Article

Nano-ZrO₂-Catalyzed Biginelli Reaction and the Synthesis of Bioactive Dihydropyrimidinones That Targets PPAR- γ in Human Breast Cancer Cells

Suresha N. Deveshegowda¹, Ji-Rui Yang², Zhang Xi³ , Omantheswara Nagaraja⁴, Kashifa Fazl-Ur-Rahman⁵, Bhanuprakash C. Narasimhachar¹, Gautam Sethi⁶, Ganga Periyasamy⁵, Mahendra Madegowda⁴ , Shobith Rangappa⁷, Vijay Pandey^{2,8} , Peter E. Lobie^{2,3,8,*} and Basappa Basappa^{1,*} 

¹ Laboratory of Chemical Biology, Department of Studies in Organic Chemistry, University of Mysore, Mysore 570006, India

² Tsinghua Berkeley Shenzhen Institute, Tsinghua Shenzhen International Graduate School, Tsinghua University, Shenzhen 518055, China

³ Shenzhen Bay Laboratory, Shenzhen 518107, China

⁴ Department of Studies in Physics, University of Mysore, Mysore 570006, India

⁵ Department of Chemistry, Central College Campus, Bangalore University, Bangalore 560001, India

⁶ Department of Pharmacology, Yong Loo Lin School of Medicine, National University of Singapore, Singapore 117600, Singapore

⁷ Adichunchanagiri Institute for Molecular Medicine, Adichunchanagiri University, Mandya 571448, India

⁸ Institute of Biopharmaceutical and Health Engineering, Tsinghua Shenzhen International Graduate School, Tsinghua University, Shenzhen 518055, China

* Correspondence: pelobie@sz.tsinghua.edu.cn (P.E.L.); salundibasappa@gmail.com (B.B.)



Citation: Deveshegowda, S.N.; Yang, J.-R.; Xi, Z.; Nagaraja, O.; Fazl-Ur-Rahman, K.; Narasimhachar, B.C.; Sethi, G.; Periyasamy, G.; Madegowda, M.; Rangappa, S.; et al. Nano-ZrO₂-Catalyzed Biginelli Reaction and the Synthesis of Bioactive Dihydropyrimidinones That Targets PPAR- γ in Human Breast Cancer Cells. *Catalysts* **2023**, *13*, 228. <https://doi.org/10.3390/catal13020228>

Academic Editors: Maciej Trejda and Lukasz Wolski

Received: 19 October 2022

Revised: 6 January 2023

Accepted: 11 January 2023

Published: 18 January 2023



Copyright: © 2023 by the authors. Licensee MDPI, Basel, Switzerland. This article is an open access article distributed under the terms and conditions of the Creative Commons Attribution (CC BY) license (<https://creativecommons.org/licenses/by/4.0/>).

Abstract: Bioactive dihydropyrimidinones (DHPs) were designed and synthesized by a multicomponent Biginelli reaction. The reaction was catalyzed by the polarized surface of nano-zirconium dioxide with partial positive charge of 0.52e at the Zr center and a negative charge of $-0.23e$ at the oxygen center. There was good corroboration between the computed and experimental ZrO₂ cell parameters and bond distances as determined by in silico and in vitro experimental methods. Since DHPs were found to target the peroxisome proliferator-activated receptor (PPAR)- γ , we tested these ligands toward MCF-7 cell toxicity, which revealed that the compounds **4d** [ethyl-4-(4'-fluoro-[1,1'-biphenyl]-4-yl)-6-methyl-2-oxo-1,2,3,4-tetrahydropyrimidine-5-carboxylate] and **4e** [ethyl-4-(3'-methoxy-[1,1'-biphenyl]-4-yl)-6-methyl-2-oxo-1,2,3,4-tetrahydropyrimidine-5-carboxylate] inhibited proliferation with IC₅₀ values of 11.8 and 15.8 μ M, respectively. Further, our bioinformatic analysis found that the active molecule **4d**, fit into the enzyme's catalytic site, almost in the same position as rosiglitazone, which was buried deep inside the cavity. In conclusion, we herein report novel DHPs which could be better structures to help explore a new class of synthetic PPAR- γ ligands.

Keywords: dihydropyrimidinone; PPAR- γ ligands; DFT calculations; zirconia; MCF-7 cells

1. Introduction

Peroxisome proliferator-activated receptor (PPAR)- γ is a transcription factor protein composed of five different domains: N-terminus, Activation Factor-1, Central DNA-binding, D, and F domains [1–4]. PPAR- γ plays a role in the development of breast cancer tumors by interacting with IGF and its downstream pathways, such as MAPK, PI3K, and the mTOR pathway, which negatively regulate the growth of cancer cells [5–8]. Furthermore, cyclin D1 suppression and p53 over expression in breast cancer cells are transcription events associated with PPAR, allowing us to create PPAR-targeting ligands [9]. PPAR- γ -activating ligands, such thiazolidinediones (TZDs, pioglitazone, and rosiglitazone, **1**), arachidonic acid, leukotriene B₄, non-esterified fatty acids, clofibrate, fenofibrate, bezafibrate, and Wy-14643, increase apoptosis and prevent tumor cells from forming new blood

vessels [8–12]. This class of compounds have a U-shaped pharmacophore that is required, with one acid group attached to a core planar ring and an extra lipophilic component, which together produce H-bonds in the PPAR- γ amino acids His449, His323, Ser289, and Tyr473 in the active site [13,14]. A poorly soluble ligands, such as phenylpropanoic acids, in solid-phase hydrogels have been used in high-throughput crystal structure determination methods to bind at the LBDs of PPAR [15]. Valeric acid, a partial agonist of PPAR- γ , promoted adipocyte differentiation, glucose uptake-related proteins, and adiponectin production by binding to the Ω loop pocket of PPAR- γ [16]. Ciglitazone, a PPAR- γ agonist, inhibited tumor growth and its associated angiogenesis, by inhibiting the phosphorylation of STAT3 and showed multiple actions, appearing as a potential candidate for treating malignant glioma [17]. It was also revealed that PPAR- γ agonists might be improved by switching out the thiazolidinedione ring for its bioisosteric groups, such as pyran, oxazolidine-2,4-dione, tetrazole, carbazole, or oxathiazoles [18–22]. The discovery of dihydropyrimidinone **2** (DHPs) as a promising PPAR- γ agonist was mostly due to the bioisosteric replacement of the thiazolidinedione ring [23]. This compound was then modified to have an extra lipophilic structure and carbonyl functionality [24–26]. We have previously shown in silico and in vitro that 5-acetyl-4-(1*H*-indol-3-yl)-6-methyl-3,4-dihydropyrimidin-2(1*H*)-one is the lead structure that targets PPAR- γ [27]. We therefore expanded our research in this paper by affixing lipophilic and heterocyclic rings (R) at the third and fourth positions in **3** and found that some of the active DHPs as novel scaffolds acted as PPAR- γ ligands (Figure 1).

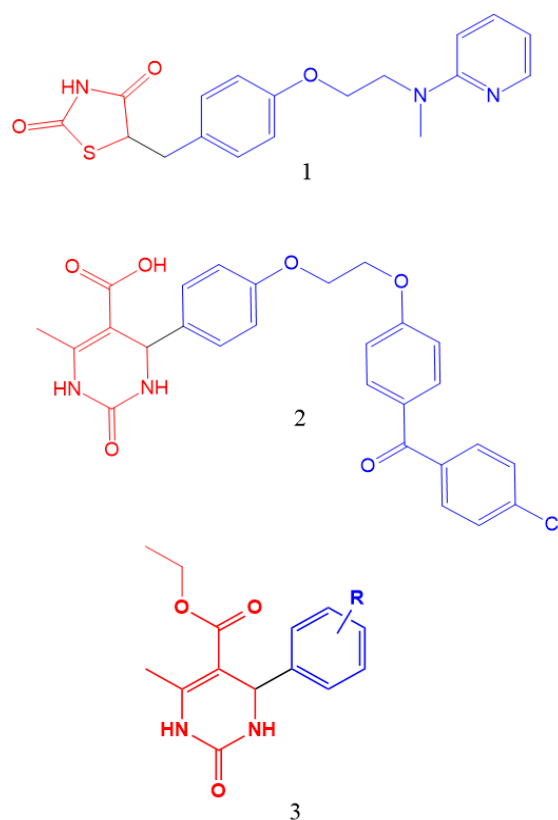


Figure 1. Generation of DHPs as PPAR- γ agonists.

2. Results and Discussions

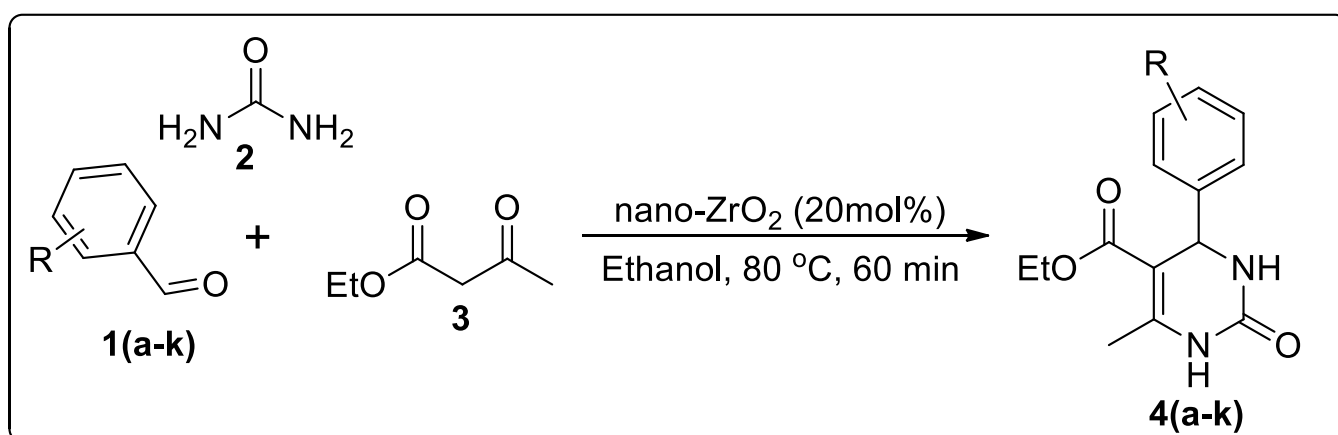
2.1. Chemical Synthesis of Dihydropyrimidinones

We initially employed a Biginelli reaction to synthesize bioactive DHPs using nano-ZrO₂ as a catalyst since the increased surface area in nano-materials allows organic substrates and reagents to selectively react to form products, which in-turn can then diffuse freely from the reaction catalytic sites [28]. Biginelli reactions are well known as a one-pot condensation reactions of an aldehyde (**1a–k**), urea (**2**), and β -keto ester (**3**) to obtain DHPs,

a medicinally useful class of heterocycle [29]. A nano-catalysts can run many organic reactions with a negligible amount, as such these materials are widely used in green synthesis, which gives significant, selective results, eventually the formation of side products is limited by various heterocyclic ring formation procedures [30,31]. Since ZrO_2 nanoparticles are less studied in the area of heterocyclic ring-forming reactions, we recently reported the synthesis and characterization of nano- ZrO_2 and also utilized this metal composite in the multi-component synthesis of bioactive pyranopyrazoles to target cyclin dependent kinase 1 in human breast cancer cells [32].

Initially, the Biginelli reaction was carried out for compound **4a** via refluxing **1a**, urea (**2**), ethyl acetoacetate (**3**), and 20 mol% of the nano ZrO_2 catalyst in an ethanol solvent for 60 min, achieving a significant yield (90%). Moreover, increasing the amount of catalyst had no effect on the percentage yield. After reaction completion, the crude was filtered and the filtrate containing the catalyst was recovered, dried and reused five more times. The only disadvantage in using the nano- ZrO_2 catalyst would be in its large-scale use, as it will be difficult to manufacture it in large quantities and reduce the heterogeneity in the size of the metal composites.

Herein, we conducted a multi-component Biginelli reaction using nano- ZrO_2 and succeeded in obtaining bioactive Biginelli products (Scheme 1, Table 1). The resultant product was completely characterized using highly advanced analytical techniques (Supplementary Materials).



Scheme 1. Synthetic scheme for the preparation of DHPs.

Table 1. Tabular representation of the Biginelli reactants and products used in this study and their cytotoxicity data on human breast cancer MCF-7 cells. IC_{50} is a measure from three independent experimental wells.

SI No	Aldehyde	Product	MCF-7 (IC_{50} in μM)	MCF-10A (IC_{50} in μM)
1			40.06 ± 1.60	>100

Table 1. Cont.

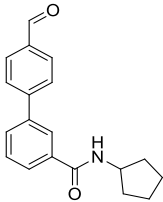
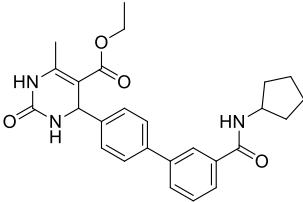
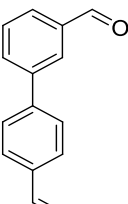
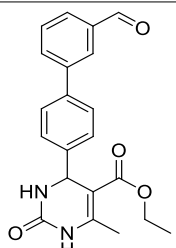
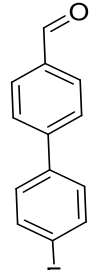
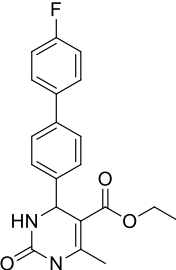
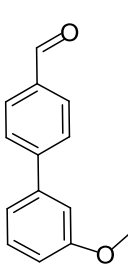
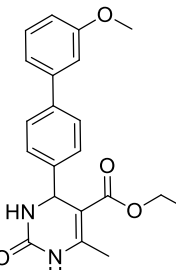
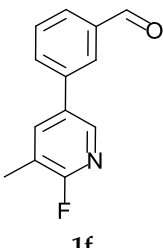
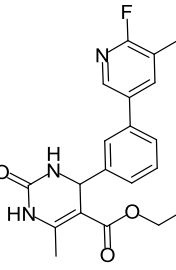
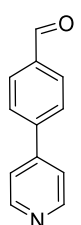
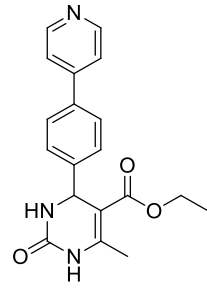
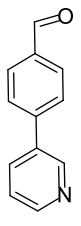
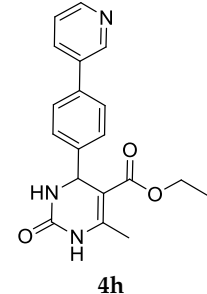
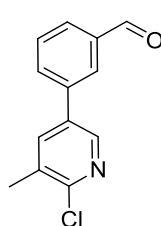
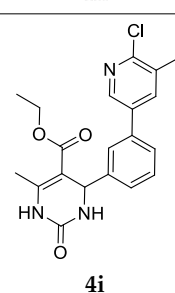
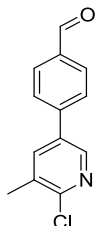
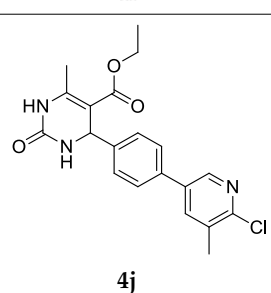
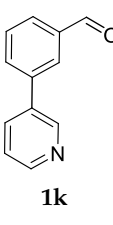
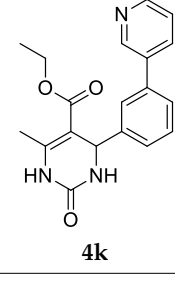
SI No	Aldehyde	Product	MCF-7 (IC ₅₀ in μM)	MCF-10A (IC ₅₀ in μM)
2	 1b	 4b	21.20 \pm 1.33	51.8
3	 1c	 4c	26.29 \pm 1.42	>100
4	 1d	 4d	11.88 \pm 1.08	>100
5	 1e	 4e	15.82 \pm 1.20	>100
6	 1f	 4f	62.83 \pm 1.80	-

Table 1. Cont.

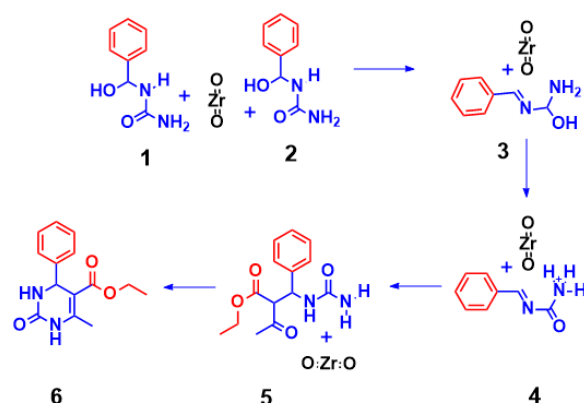
SI No	Aldehyde	Product	MCF-7 (IC ₅₀ in μM)	MCF-10A (IC ₅₀ in μM)
7	 1g	 4g	61.70 ± 1.79	-
8	 1h	 4h	40.03 ± 1.61	-
9	 1i	 4i	57.13 ± 1.76	-
10	 1j	 4j	73.65 ± 1.87	-
11	 1k	 4k	79.71 ± 1.90	-
12	Olaparib		3.28 ± 0.20	-

2.2. Mechanistic Investigation of Biginelli Reaction

Soon after the report of the original Biginelli reaction, several methods have been reported as modifications using different catalysts, and advancements in the Biginelli reaction

was made by improving the percentage yields of DHPs, by using less hazardous reaction conditions, or by facile isolation of DHPs from the reaction mixture [33,34]. The Biginelli reaction mechanism has been precisely studied in which the limiting step was found to be an in situ aldol condensation, followed by an additional urea molecule condensation with the reactive mixture to give the corresponding DHPs. Further, the artificial force-induced reaction method has been systematically used to analyze the reaction mechanism of the Biginelli reaction, which revealing that the first step was confirmed by the condensation of urea and benzaldehyde, followed by the addition of ethyl acetoacetate via a second urea molecule catalysis [35]. Additionally, a simple, economic, pressurized, and erbium trichloride hexahydrate-catalyzed solvent-free reaction was carried out using Q-tube equipment to produce Biginelli reaction products [36]. In addition, a Biginelli reaction was carried out under solvent-free condition using an imidazolium and sulfonic acid-decorated (Bronsted acid) catalyst system [37]. Therefore, we performed a DFT calculation in order to evaluate the role of nano-ZrO₂ in the mechanistic aspects of the Biginelli reaction.

For this purpose, we initially optimized the ZrO₂ structure, where 3D periodicity was removed by extending 10 Å in the z-direction and the organic molecule was placed on the surface. During the optimization, the ZrO₂ surface atomic positions were restrained and the organic molecules were allowed to relax. The adsorbent had three functional units (-OH, NH₂ and C=O) in the tail prone to interaction with the ZrO₂ surface. The conformational search led to two stable orientations (molecule 1 and 2) in Scheme 2. In orientation 1, the OH and NH₂ groups simultaneous interacted with the O of the ZrO₂ surface with bond distances of $d_{\text{HNH}\dots\text{O}_{\text{Zr}}}$: 1.24 and 1.56 Å and $d_{\text{OH}\dots\text{O}_{\text{Zr}}}$: 1.62 Å. The six-membered ring presented perpendicular to the surface at a distance of 1.35 Å. The calculations suggested that the electronegativity of oxygen was prone to adsorb a proton from the NH₂ group of the organic molecule. In orientation 2, the carbonyl group was parallel to the surface, allowing the -NH₂ group to interact with the surface. The OH group interacted with surface by 1.96 Å. Hence, orientation 2 reverted back to the molecule orientation 1 during the optimization. The orientation of molecule 2's energies was calculated by restraining the ligand's positions. The orientation of molecule 1 was more stable with 0.56 eV than 2. The optimized geometries are given in Figure 2. The adsorption energies for orientation 1 was larger than orientation 2. The adsorption of the organic molecules increased the Fermi energy (E_{Fermi} of ZrO₂ surface: -6.43 eV; ZrO₂-organic molecule 1: -5.73 eV and ZrO₂-organic molecule 2: -5.54 eV) by 0.69 and 0.89 eV for orientations 1 and 2, respectively. The interaction between the organic molecules and the surface were also found to decrease the band gap to 0.01 eV irrespective of the orientations. This confirms the orbital overlap and thereby the chemical bonding between the adsorbent and adsorbate. The reduction and removal of water molecule led to molecule 3, where the six-member ring became parallel to the surface making pi-stacking interactions with ~1.60 to 2.17 Å. However, as observed in orientation 1, the NH₂ group strongly bound to the oxygen of the ZrO₂ with a distance of 1.12 Å. The species was stable on the surface with a negative adsorption energy of -1.82 eV. The presence of the NH₃ group in molecule 4 did not prefer to interact with the ZrO₂ through the six-member ring. The two protons of the NH₃ group strongly interacted with the oxygen on the ZrO₂ surface. The computed negative adsorption energy of -1.75 eV shows the stability of molecule 4 on the surface. The increase in the bulkiness of the side chains of molecules 5 weakened the interaction between the surface and molecule, where only H-bonding interactions were observed with a distance of 2.36 Å. Interestingly, the steric side chain allowed the C=O to interact with the Zr surface and presented at a distance of 1.83 Å. However, a negative adsorption energy (-0.32 eV) was observed. Molecule 6 was adsorbed on to the surface through weak interaction with an adsorption energy of -0.08 eV. The increase in bond distance between the ZrO₂ and molecule 6 facilitated the release of the product without the transition state. The decrease in interaction was found to stabilize the Fermi orbital with more negative energy.



Scheme 2. Biginelli reaction intermediates (molecules 1–5) and product (molecule 6) representations to understand the reaction mechanism.

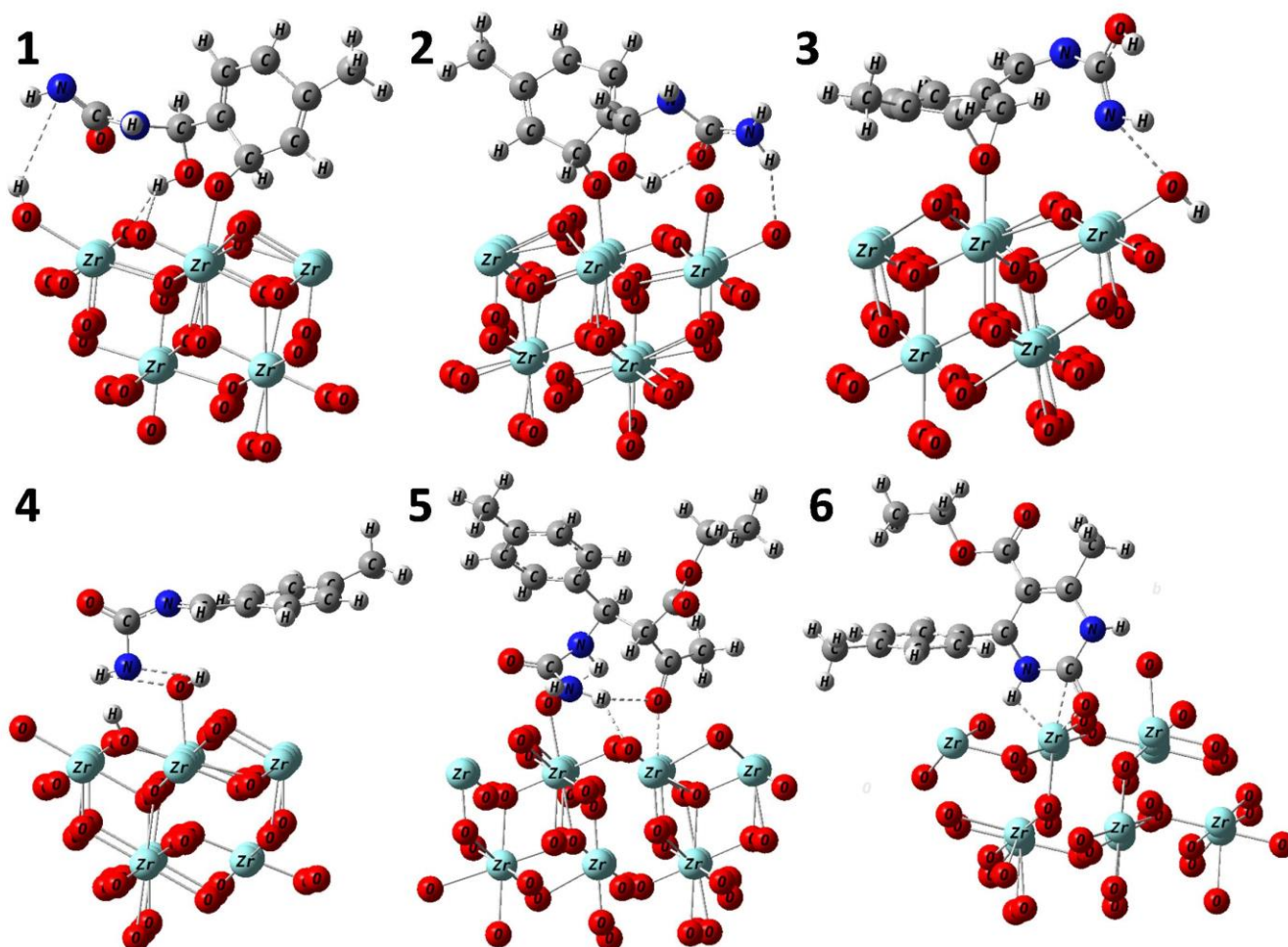


Figure 2. Optimized geometries of the surface-adsorbed molecules 1–6.

In conclusion, we computationally found that the nano-ZrO₂ surface is a polarized surface with a partial positive charge of 0.52e at the Zr center and a negative charge of −0.23e at the oxygen center (Table 2). There was good corroboration between the computed and experimental ZrO₂ cell parameters and bond distances, as given in Table 3 and Scheme 2, which supports the method adopted in this work.

Table 2. Adsorption energy calculations for the Biginelli intermediates and products.

Molecule	E_{Fermi} (eV)	Band Gap (eV)	Adsorption Energy (E_{ads} , eV)
ZrO ₂ Surface	−6.43	0.02	-
ZrO ₂ Surface-Molecule 1	−5.72	0.01	−3.31
ZrO ₂ Surface-Molecule 2	−5.54	0.01	−2.75
ZrO ₂ Surface-Molecule 3	−5.77	0.01	−1.82
ZrO ₂ Surface-Molecule 4	−5.98	0.01	−1.75
ZrO ₂ Surface-Molecule 5	−6.01	0.01	−0.32
ZrO ₂ Surface-Molecule 6	−6.21	0.01	−0.08

Table 3. Comparison between the experimental and calculated cell parameters and bond distance for bulk m-ZrO₂.

Cell Parameter/Bond Length	Experimental	Calculated
a (Å)	5.21	5.1147
b (Å)	5.26	5.1299
c (Å)	5.37	5.1149
α (°)	90.00	90.00
β (°)	80.53	90.18
γ (°)	90.00	90.00
V (Å ³)	145.2	134.15
Zr-O (Å)	2.021 1.952	2.225, 2.223 2.221, 2.220

2.3. DHPs Inhibits the Proliferation of MCF-7 Cells

MDG 548 (thioxopyrimidindione) was discovered as a selective PPAR- γ scaffold via a robust, integrated and “tier”-based throughput virtual screening method with a special focus on the retrieval of novel bioactive chemical scaffolds for PPAR- γ [38]. Using a Alamar Blue assay, we screened 11 DHPs against the proliferation of MCF-7 cells. In the assay condition, Olaparib was used as a positive control. Among the tested DHPs, compounds **4b–e** inhibited the proliferation of MCF-7 cells with IC₅₀ values of 11.8, 15.8, 21.2, and 26.2 μM , respectively (Supplementary Materials). The biphenyl rings containing DHPs, whose substituents such as cyclopentylamide, carbaldehyde, fluorine, and methoxy groups or atoms at the 4th or 3rd positions were found to be responsible for the bioactivity. Further, we performed a cytotoxicity experiment using the MCF-10A cell line, a non-tumorigenic epithelial cell line, in order to evaluate the selectivity of lead DHPs anti-cancer activity. The results of the analysis revealed that the compounds were non-toxic up to 100 μM , indicating an anti-cancer effect in human breast cancer cells (Supplementary Materials).

2.4. Bioinformatic Analysis of DHPs That Targets PPAR- γ in MCF-7 Cells

Since rosiglitazone has been established as a potent PPAR- γ agonist and its co-crystal structure resolved, we herein conducted a bioinformatic analysis to understand the DHP binding affinity toward PPAR- γ , using the reported co-crystal structure (PDB ID:4EMA). In silico molecular simulations of compound **4d** into the active site of PPAR- γ was conducted. Re-docking of co-crystallized ligands into the active site of PPAR- γ replicated all the key interactions accomplished by the co-crystallized ligand with the key amino acids in the active site, as shown in Figures 3 and 4 [39], indicating that the used setup was suitable for the docking study. Molecular docking of compound **4d** in PPAR- γ revealed an optimal binding mode defined by the affinity of the minimum Gibbs binding energy of

−8.9 kcal/mole. As shown in Figure 5, compound **4d** fitted into the PPAR- γ active site in almost the same position as the rosi, buried deep inside the cavity (Figure 6). Ser289 formed a hydrogen bond with the −NH group of the pyrimidinone ring. Besides the hydrogen bond interaction, compound **4d** linked to the PPAR- γ amino acid residues Arg288 and Tyr327 via cation– π and π – π interactions, respectively, as shown in Figure 7. Furthermore, hydrophobic interactions with residues Cys285, Ser289, Arg288, Ala292, Ile326, Tyr327, Met329, Leu330, Phe363, Met364, and His449 were observed, increasing the complex's stability (Figure 8).

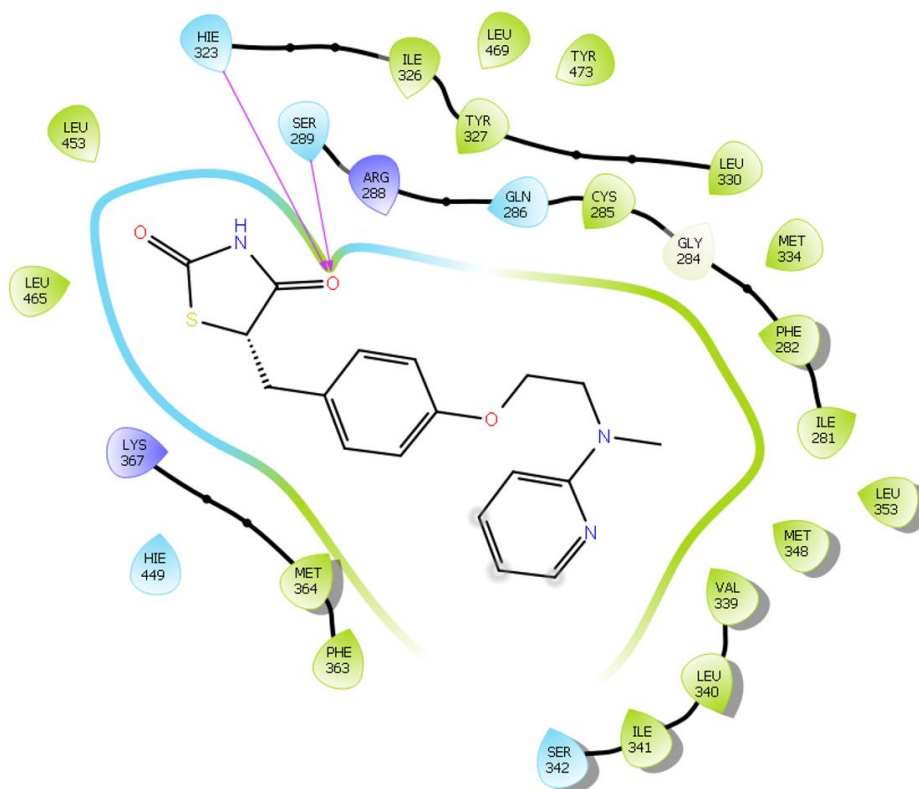


Figure 3. 2D interaction of the cross-docked ligand (rosi) with the receptor molecule.

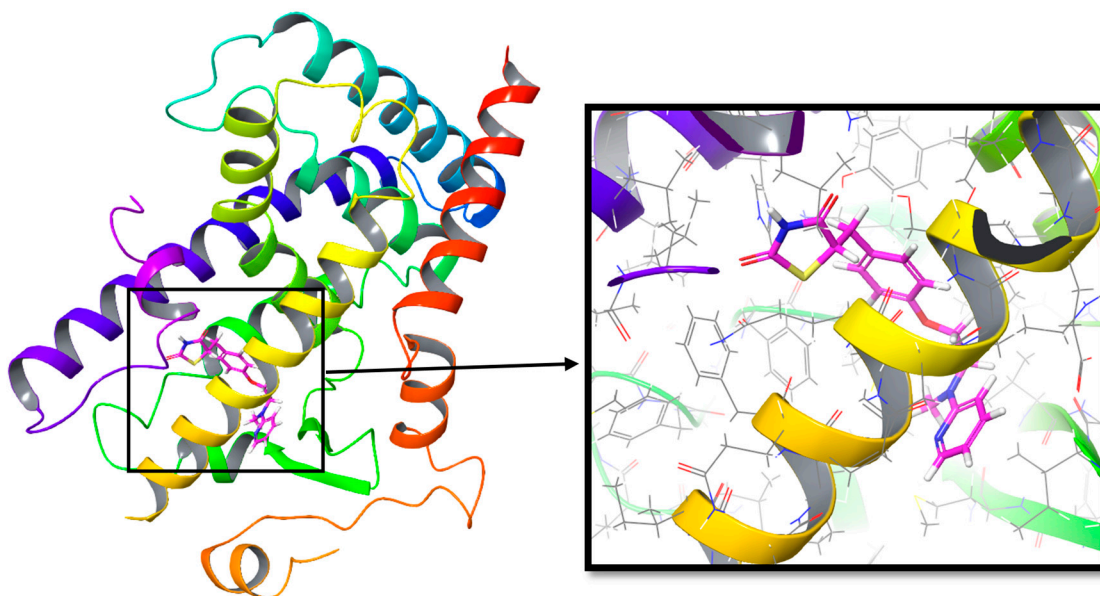


Figure 4. Cartoon representation of rosi (magenta) in the active site of PPAR- γ .

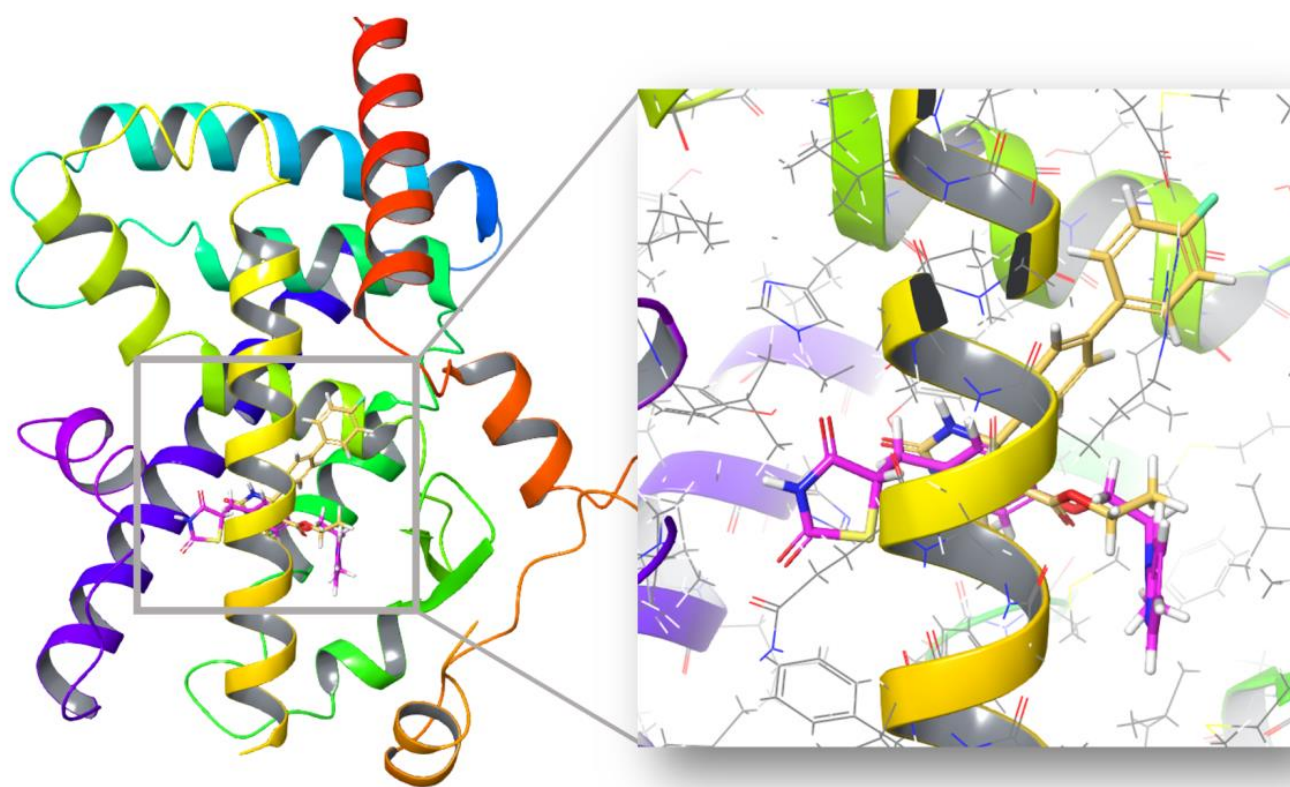


Figure 5. Cartoon representation of the cross-docked ligand (CL) and protein complex.

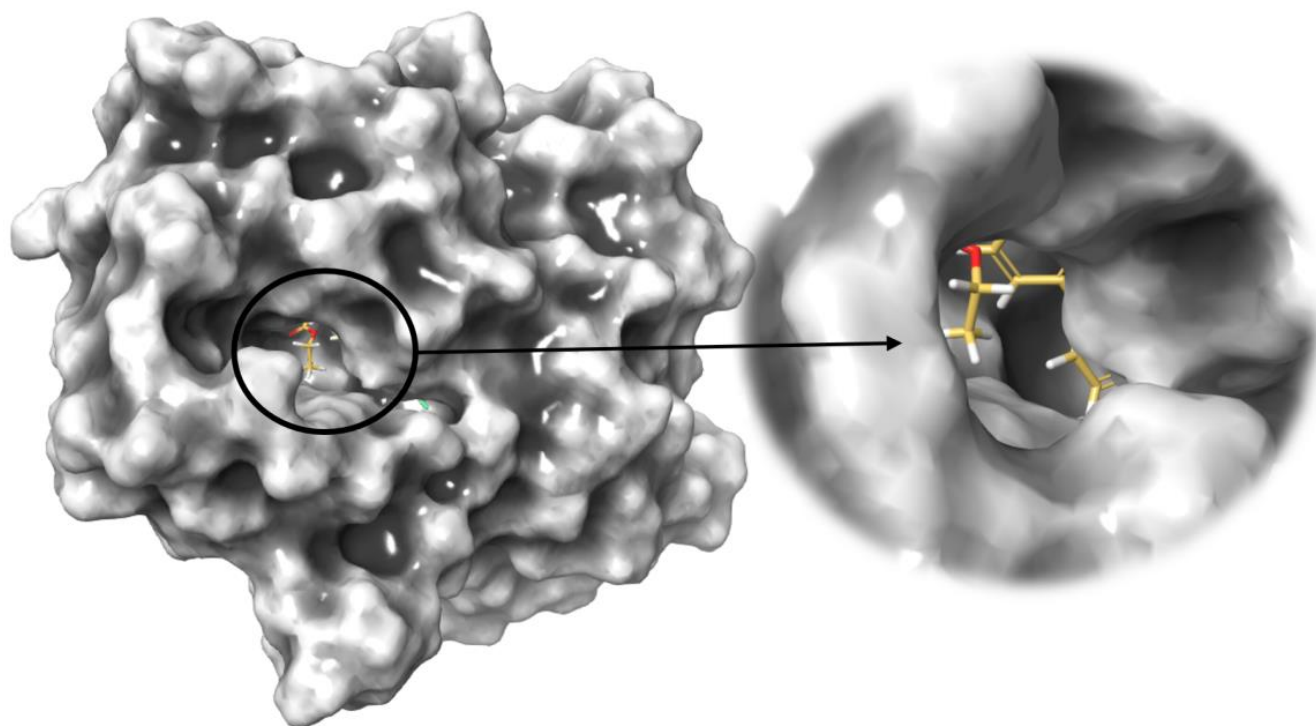


Figure 6. 3D surface view of the PPAR- γ and **4d** ligand complex.

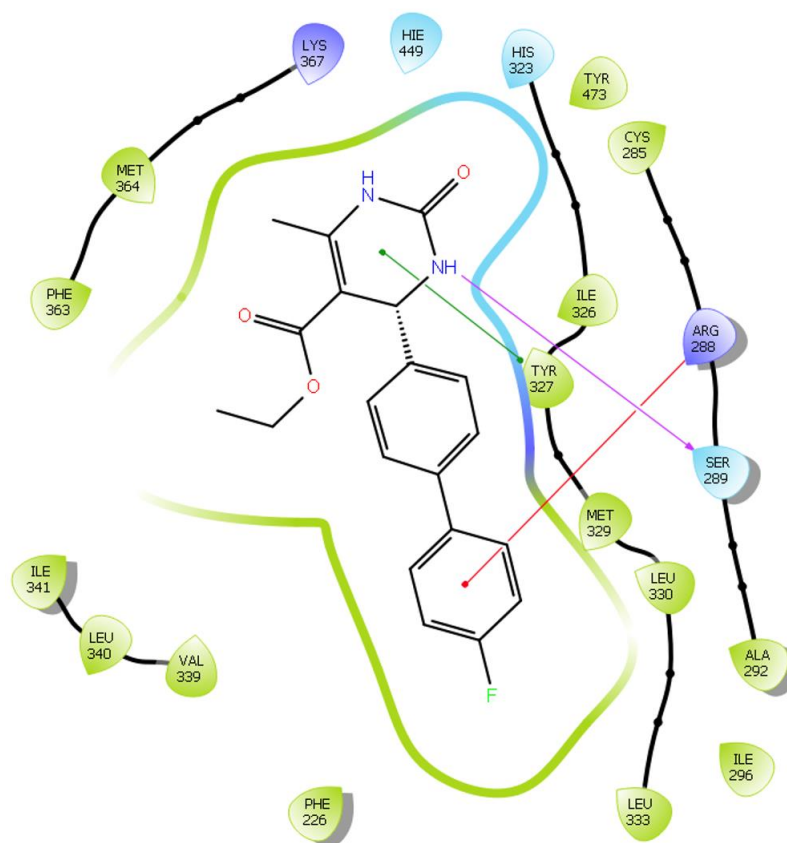


Figure 7. 2D interaction diagram of **4d** with the active site residues of PPAR- γ .

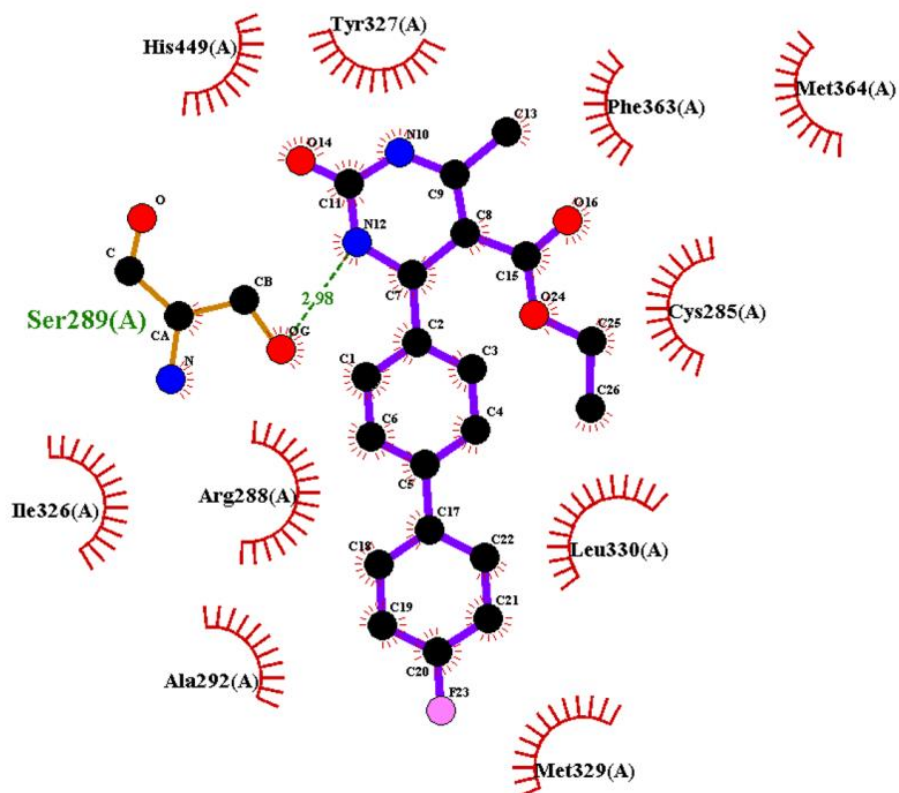


Figure 8. Ligplot images showing the hydrophobic interactions of **4d** with the receptor PPAR- γ .

3. Materials and Methods

3.1. Chemistry

The chemicals and solvents used for the reactions were purchased from Sigma-Aldrich (St. Louis, MO, USA). Pre-coated silica gel TLC plates were used to monitor the completion of the reaction. ^1H - and ^{13}C -NMR was recorded on an Agilent NMR spectrophotometer (400 and 500 MHz, Santa Clara, CA, USA); TMS and CDCl_3 were used as an internal standard and solvent, respectively. Chemical shifts are expressed as ppm.

3.2. General Procedure for the Synthesis of the Substituted Dihydropyrimidinones (DHPs)

Different substituted aldehydes (**1a–k**) were dissolved in ethanol in a 100 mL round-bottomed flask. Subsequently, urea (**2**), ethyl acetoacetate (**3**), and nano-ZrO₂ (20 mol%) were added in equimolar amounts to the above solution. Stirring was continued and the reaction was refluxed at 80 °C for up to 60 min. Completion of the reaction was monitored by silica-coated TLC and filtered to recover the catalyst for reuse, the collected reaction mass solution was added to ice-cold water and white solid products (**4a–k**) were formed, which were filtered using Whatman filter paper and recrystallized with hot ethanol.

3.3. Ethyl-4-(4-(6-fluoro-5-methylpyridin-3-yl)phenyl)-6-methyl-2-oxo-1,2,3,4-tetrahydropyrimidine-5-carboxylate (**4a**)

^1H -NMR (500 MHz, CDCl_3): δ 8.11 (s, 1H), 7.79 (s, 1H), 7.40 (d, $J = 8.0$ Hz, 2H), 7.35 (d, $J = 8.1$ Hz, 2H), 5.68 (s, 1H), 5.39 (s, 1H), 4.11–4.05 (m, 2H), 2.30 (s, 3H), 2.28 (s, 3H), 1.13 (t, 7.0 Hz, 3H); ^{13}C -NMR (126 MHz, CDCl_3): δ 165.5, 162.8, 153.0, 146.3, 143.4, 142.8, 140.2, 136.6, 134.3, 127.6, 60.2, 55.4, 18.9, 14.6, 14.9; LCMS (ESI): m/z for $\text{C}_{20}\text{H}_{20}\text{FN}_3\text{O}_3$, calcd 369.39; found: 370.15 $[\text{M} + \text{H}]^+$.

3.4. Ethyl-4-(3'-(cyclopentylcarbamoyl)-[1,1'-biphenyl]-4-yl)-6-methyl-2-oxo-1,2,3,4-tetrahydropyrimidine-5-carboxylate (**4b**)

^1H -NMR (500 MHz, CDCl_3): δ 7.88 (s, 1H), 7.63 (dd, $J = 23.5, 7.5$ Hz, 2H), 7.50 (d, $J = 7.5$ Hz, 2H), 7.43 (t, $J = 7.5$ Hz, 1H), 7.36 (d, $J = 7.5$ Hz, 2H), 6.23 (s, 1H), 5.42 (s, 1H), 4.40 (dd, $J = 13.8, 7.0$ Hz, 1H), 4.11–4.05 (m, 2H), 2.34 (s, 3H), 2.07 (dt, $J = 11.7, 5.8$ Hz, 2H), 1.72 (s, 4H), 1.49 (m, 2H), 1.16 (t, $J = 6.9$ Hz, 3H); ^{13}C -NMR (126 MHz, CDCl_3): δ 167.2, 165.6, 153.3, 146.4, 143.1, 141.0, 139.9, 135.5, 129.8, 128.9, 127.5, 127.1, 125.6, 101.2, 60.1, 55.3, 51.7, 33.2, 23.8, 18.8, 14.2; LCMS (ESI): m/z for $\text{C}_{20}\text{H}_{20}\text{FN}_3\text{O}_3$, calcd 447.53; found: 448.21 $[\text{M} + \text{H}]^+$.

3.5. Ethyl-4-(3'-formyl-[1,1'-biphenyl]-4-yl)-6-methyl-2-oxo-1,2,3,4-tetrahydropyrimidine-5-carboxylate (**4c**)

^1H -NMR (500 MHz, CDCl_3): δ 10.06 (s, 1H), 8.11–8.05 (m, 1H), 7.82 (ddd, $J = 17.4, 7.7, 1.2$ Hz, 1H), 7.65–7.50 (m, 2H), 7.42 (d, $J = 8.0$ Hz, 1H), 7.30 (d, $J = 5.0$ Hz, 2H), 5.87 (s, 1H), 5.45 (s, 1H), 4.10–4.03 (m, 2H), 2.36 (s, 3H), 1.18 (t, $J = 7.1$ Hz, 3H); ^{13}C -NMR (126 MHz, CDCl_3): δ 192.3, 165.6, 153.3, 146.4, 143.5, 141.5, 139.3, 136.9, 132.96, 129.52, 128.7, 128.0, 127.4, 126.6, 101.3, 60.1, 55.7, 55.4, 18.8, 14.2; LCMS (ESI): m/z for $\text{C}_{20}\text{H}_{20}\text{FN}_3\text{O}_3$, calcd 364.39; found: 365.14 $[\text{M} + \text{H}]^+$.

3.6. Ethyl-4-(4'-fluoro-[1,1'-biphenyl]-4-yl)-6-methyl-2-oxo-1,2,3,4-tetrahydropyrimidine-5-carboxylate (**4d**)

^1H -NMR (500 MHz, CDCl_3): δ 8.26 (s, 1H), 7.51–7.47 (m, 2H), 7.46 (d, $J = 8.0$ Hz, 2H), 7.37 (d, $J = 8.3$ Hz, 2H), 7.09 (t, $J = 8.7$ Hz, 2H), 5.91 (s, 1H), 5.43 (d, $J = 2.8$ Hz, 1H), 4.08–4.05 (m, 2H), 2.34 (s, 3H), 1.17 (t, $J = 7.1$ Hz, 3H); ^{13}C -NMR (126 MHz, CDCl_3): δ 165.6, 153.4, 146.4, 142.7, 139.8, 136.7, 128.6, 127.3, 127.1, 115.6, 101.3, 60.1, 55.3, 18.7, 14.2.

3.7. Ethyl-4-(3'-methoxy-[1,1'-biphenyl]-4-yl)-6-methyl-2-oxo-1,2,3,4-tetrahydropyrimidine-5-carboxylate (4e)

¹H-NMR (500 MHz, CDCl₃): δ 7.51 (d, *J* = 8.2 Hz, 2H), 7.37 (d, *J* = 8.2 Hz, 2H), 7.33 (t, *J* = 7.9 Hz, 1H), 7.13 (d, *J* = 7.7 Hz, 1H), 7.08–7.06 (m, 1H), 6.88 (dd, *J* = 8.2, 2.5 Hz, 1H), 5.81 (s, 1H), 5.43 (d, *J* = 2.4 Hz, 2H), 4.09–4.06 (m, 2H), 3.84 (s, 3H), 2.35 (s, 3H), 1.17 (t, *J* = 7.1 Hz, 3HF); ¹³C-NMR (126 MHz, CDCl₃): δ 165.6, 159.8, 153.3, 146.2, 142.8, 140.7, 129.8, 128.4, 127.5, 127.0, 119.6, 112.7, 101.4, 60.1, 55.3, 18.8, 14.2; LCMS (ESI): *m/z* for C₂₁H₂₂N₂O₄, calcd 366.41; found: 367.15 [M + H]⁺.

3.8. Ethyl-4-(3-(6-fluoro-5-methylpyridin-3-yl)phenyl)-6-methyl-2-oxo-1,2,3,4-tetrahydropyrimidine-carboxylate (4f)

¹H-NMR (500 MHz, CDCl₃): δ 8.21 (s, 1H), 8.16 (s, 1H), 7.72–7.70 (m, 1H), 7.43 (s, 1H), 7.40–7.39 (m, 1H), 7.34 (d, *J* = 2.0 Hz, 1H), 5.99 (s, 1H), 5.46 (d, *J* = 2.8 Hz, 1H), 4.08–4.04 (m, 2H), 2.34 (s, 3H), 2.32 (s, 3H), 1.15–1.13 (m, 3H); ¹³C-NMR (126 MHz, CDCl₃): δ 165.6, 153.28, 146.6, 144.5, 142.8, 140.3, 137.3, 134.6, 129.5, 128.7, 126.6, 126.2, 125.3, 119.4, 101.0, 60.1, 55.6, 18.8, 14.6, 14.8.

3.9. Ethyl-6-methyl-2-oxo-4-(4-(pyridin-3-yl)phenyl)-1,2,3,4-tetrahydropyrimidine-5-carboxylate (4g)

¹H-NMR (400 MHz, CDCl₃): δ 8.54 (s, 2H), 7.84 (s, 1H), 7.61 (dd, *J* = 21.5, 7.3 Hz, 4H), 7.43 (s, 1H), 6.26 (s, 1H), 5.62 (s, 1H), 4.25 (d, *J* = 6.9 Hz, 2H), 2.52 (s, 3H), 1.35 (t, *J* = 6.9 Hz, 3H); LCMS (ESI): *m/z* for C₂₁H₂₂N₂O₄, calcd 337.37; found: 338.14 [M + H]⁺.

3.10. DFT Calculations

The structure and activity of all the molecules on ZrO₂ surface was studied by density functional theoretical (DFT) methods. The structure model for the calculations was generated based on the experimental crystal structures. These models were optimized using the Kohn–Sham self-consistent DFT method as implemented in the SIESTA (Spanish Initiative for Electronic Simulations with Thousands of Atoms) package [40], which consists of localized molecular-orbital basis sets. The exchange–correlation functional, Exc using generalized gradient approximation (GGA) of the Perdew–Burke–Ernzerhof (PBE) [41] and Troullier–Martins norm-conserving pseudo potentials in the Kleinman–Bylander form was used to describe all atoms in the calculation. A double-zeta basis (DZP) set with a polarization orbital was included for all atoms and a pseudo atomic orbital basis set was used for Zr with a real-space mesh cut-off of 300 Ry. Most of the calculations reported so far on adsorption and reactivity of molecules on zirconium were performed on the monoclinic phase which is stable at room temperature. The monoclinic ZrO₂ (111) surface was exposed by a 2 × 1 unit cell with three layers in the slab model. The layers were allowed to relax during optimization. The sampling of the Brillouin zone was performed with 3 × 3 × 1 k-point grids. A vacuum region of 10 Å is placed over the slab to avoid interactions with the neighboring unit cell. All models were relaxed until the interatomic force was 0.01 eV Å⁻¹. The atomic coordinates were relaxed with convergence criteria of 0.05 eV for energy and 0.05 Å for displacement. Note that surface states only contribute from atoms close to the surface of slab. For calculation of the binding energies of all reactant molecules, the molecule was placed on top of the surface and the top layer was allowed to interact with the adsorbate while the bottom layers were constrained. The adsorbate molecule was located above the surface at distances that were chosen to be within the range of physical interactions but longer than the corresponding chemical bond distances. The adsorption energies, Δ*E*_{ads} were calculated by, Δ*E*_{ads} = *E*_{adsorbate/ZrO₂} − (*E*_{adsorbate} + *E*_{slab}) where, Δ*E*_{ads} is the adsorption energy, *E*_{adsorbate/ZrO₂} is the energy of the ZrO₂ slab with adsorbate molecules adsorbed on the surface, *E*_{adsorbate} is the energy of adsorbate in the gas phase, and *E*_{slab} is the energy of the ZrO₂ slab. Force constants were evaluated in each case to confirm the energy minimum and transition states (single imaginary frequency). The reaction energy (Δ*H*) and activation barrier (*E*_a) for a reaction as R → P on the ZrO₂ surface were calculated based on the following formula: Δ*H* = *E*(slab + P) − *E*(slab + R),

$E_a = E(\text{slab} + \text{TS}) - E(\text{slab} + \text{R})$, where $E(\text{slab} + \text{R})$ is the total energy of the reactants on the ZrO_2 surface, and $E(\text{slab} + \text{P})$ is the total energy of the products on the ZrO_2 surface, and $E(\text{slab} + \text{TS})$ is the total energy of the transition states on the ZrO_2 surface. For adsorption and reaction energy, a negative value denotes that the process is exothermic, and a positive value denotes that it is endothermic.

3.11. Cell Viability Assay

MCF-7 cells were purchased from Procell Life Science and Technology. Around 2000 cells of MCF-7 were cultured in MEM or Leibovitz's L-15 medium containing 2% FBS and maintained at 37 °C in a 5% CO_2 atmosphere. DHPs were dissolved in DMSO. A series of DHPs were applied to the MCF-7 cells in 96-well plates for 12 h followed by 72 h of treatment with or without DHPs at concentrations of 0, 0.01, 0.1, 10, 100, and 1000 μM . A further 4 h were spent incubating the Alamar Blue assay reagent. According to the established protocol, the IC_{50} values of the compounds were determined in the absence and presence of DHPs [42–62].

3.12. Bioinformatics Analysis

Molecular docking experiments were carried out using Auto Dock Tools 1.5.7 (ADT) [63]. The X-ray crystallographic structure of PPAR- γ (PDB ID: 4EMA) was obtained from the RCSB online database (<http://www.rcsb.org> (accessed on 11 March 2022)). The receptor was stripped of water molecules, non-bonded inhibitors, and cofactors. The protein was then edited by adding polar hydrogen atoms and Kollman charges and saved in the same pdbqt format. The co-crystallized ligand (CL) and the synthesized compound **4d** were subjected to molecular docking analysis. The ADT program processed and saved the ligands in the pdbqt format for docking. All the ligand torsions were made rotatable. Docking was carried out, and the pose with the lowest binding energy was chosen. Analysis and visualization of the docking results were done using the Maestro (v2020.4; Avid Technology: New York, NY, USA, 2020) [64] and the LigPlot+ (v.2.2.5; EMBL-EBI: Cambridgeshire, UK, 2011) programs [65].

4. Conclusions

In conclusion, DHPs were synthesized by a multi-component Biginelli reaction catalyzed by nano-zirconium dioxide. The products were tested for MCF-7 cell toxicity, which inhibited the MCF-7 proliferation. Further, our bioinformatic analysis found that the active molecule fit into the enzyme's catalytic site, in almost the same position as rosiglitazone, which was buried deep inside the cavity.

Supplementary Materials: The following supporting information can be downloaded at: <https://www.mdpi.com/article/10.3390/catal13020228/s1>, ^1H NMR, ^{13}C NMR and Mass spectrums of products **4**; Log curves of synthesized compounds on MCF-7 cancer cells; Log curves of synthesized compounds on MCF-10A non-cancerous cells.

Author Contributions: S.N.D., J.-R.Y., O.N., Z.X., K.F.-U.-R. and B.C.N., performed the experiments. M.M., G.P., V.P., S.R. and G.S. supervised the research. P.E.L. and B.B., designed the experiments, provided the resources and wrote the manuscript. All authors have read and agreed to the published version of the manuscript.

Funding: This work was supported by Vision Group on Science and Technology (CESEM, GRD-637), Government of Karnataka. This work was also supported by the Shenzhen Key Laboratory of Innovative Oncotherapeutics (ZDSYS20200820165400003) (Shenzhen Science and Technology Innovation Commission), China; Shenzhen Development and Reform Commission Subject Construction Project ([2017]1434), China; Overseas Research Cooperation Project (HW2020008) (Tsinghua Shenzhen International Graduate School), China; Tsinghua University Stable Funding Key Project (WDZC20200821150704001); the Shenzhen Bay Laboratory (21310031), China and TBSI Faculty Start-up Funds, China. Thanks for providing fellowship from OBC Cell, University of Mysore, Karnataka to S.N.D., and B.C.N.

Data Availability Statement: Not applicable.

Conflicts of Interest: The authors declare no conflict of interest.

References

1. Tontonoz, P.; Spiegelman, B.M. Fat and Beyond: The Diverse Biology of PPAR γ . *Annu. Rev. Biochem.* **2008**, *77*, 289–312. [[CrossRef](#)] [[PubMed](#)]
2. Heudobler, D.; Rechenmacher, M.; Lüke, F.; Vogelhuber, M.; Pukrop, T.; Herr, W.; Ghibelli, L.; Gerner, C.; Reichle, A. Peroxisome Proliferator-Activated Receptors (PPAR) γ Agonists as Master Modulators of Tumor Tissue. *Int. J. Mol. Sci.* **2018**, *19*, 3540. [[CrossRef](#)]
3. Liu, J.-J.; Liu, P.-Q.; Lin, D.-J.; Xiao, R.-Z.; Huang, M.; Li, X.-D.; He, Y.; Huang, R.-W. Downregulation of cyclooxygenase-2 expression and activation of caspase-3 are involved in peroxisome proliferator-activated receptor- γ agonists induced apoptosis in human monocyte leukemia cells in vitro. *Ann. Hematol.* **2006**, *86*, 173–183. [[CrossRef](#)] [[PubMed](#)]
4. Weng, J.-R.; Bai, L.-Y.; Chiu, C.-F.; Hu, J.-L.; Chiu, S.-J.; Wu, C.-Y. Cucurbitane Triterpenoid from *Momordica charantia* Induces Apoptosis and Autophagy in Breast Cancer Cells, in Part, through Peroxisome Proliferator-Activated Receptor γ Activation. *Evid.-Based Complement. Altern. Med.* **2013**, *2013*, 935675. [[CrossRef](#)] [[PubMed](#)]
5. El Gazzar, W.B.; Allam, M.M.; Shaltout, S.A.; Mohammed, L.A.; Sadek, A.M.; Nasr, H.E. Pioglitazone modulates immune activation and ameliorates inflammation induced by injured renal tubular epithelial cells via PPAR γ /miRNA-124/STAT3 signaling. *Biomed. Rep.* **2022**, *18*, 2. [[CrossRef](#)]
6. Belfiore, A.; Genua, M.; Malaguarnera, R. PPAR- γ Agonists and Their Effects on IGF-I Receptor Signaling: Implications for Cancer. *PPAR Res.* **2009**, *2009*, 830501. [[CrossRef](#)]
7. Waseem, D.; Khan, G.M.; Haq, I.-U.; Syed, D.N. Dibutylstannanediyyl (2Z,2'Z)-bis(4-(benzylamino)-4-oxobut-2-enoate) inhibits prostate cancer progression by activating p38 MAPK/PPAR α /SMAD4 signaling. *Toxicol. Appl. Pharmacol.* **2022**, *449*, 116127. [[CrossRef](#)]
8. Hsu, P.-C.; Hsu, C.-C.; Hsia, Y.-J.; Kuo, C.-Y. Chrysophanol Suppresses Cell Growth via mTOR/PPAR- α Regulation and ROS Accumulation in Cultured Human Tongue Squamous Carcinoma SAS Cells. *Curr. Issues Mol. Biol.* **2022**, *44*, 1528–1538. [[CrossRef](#)]
9. Han, S.W. Anticancer actions of PPAR γ ligands: Current state and future perspectives in human lung cancer. *World J. Biol. Chem.* **2010**, *1*, 31–40. [[CrossRef](#)]
10. Ahmadian, M.; Suh, J.M.; Hah, N.; Liddle, C.; Atkins, A.R.; Downes, M.; Evans, R.M. PPAR γ signaling and metabolism: The good, the bad and the future. *Nat. Med.* **2013**, *19*, 557–566. [[CrossRef](#)]
11. Xu, Y.; Denning, K.L.; Lu, Y. PPAR α agonist WY-14,643 induces the PLA2/COX-2/ACOX1 pathway to enhance peroxisomal lipid metabolism and ameliorate alcoholic fatty liver in mice. *Biochem. Biophys. Res. Commun.* **2022**, *613*, 47–52. [[CrossRef](#)] [[PubMed](#)]
12. Kostapanos, M.; Elisaf, M.; Mikhailidis, D. Pioglitazone and Cancer: Angel or Demon? *Curr. Pharm. Des.* **2013**, *19*, 4913–4929. [[CrossRef](#)] [[PubMed](#)]
13. Mochizuki, K.; Suzuki, T.; Goda, T. PPAR α and PPAR δ Transactivity and p300 Binding Activity Induced by Arachidonic Acid in Colorectal Cancer Cell Line Caco-2. *J. Nutr. Sci. Vitaminol.* **2008**, *54*, 298–302. [[CrossRef](#)] [[PubMed](#)]
14. Vidović, D.; Busby, S.A.; Griffin, P.R.; Schürer, S.C. A Combined Ligand- and Structure-Based Virtual Screening Protocol Identifies Submicromolar PPAR γ Partial Agonists. *Chemmedchem* **2010**, *6*, 94–103. [[CrossRef](#)] [[PubMed](#)]
15. Oyama, T. Toward High-throughput Crystal Structure Determination of PPAR Ligand-binding Domains in Complexes with Less Soluble Ligands. *Yakugaku Zasshi J. Pharm. Soc. Jpn.* **2022**, *142*, 1353–1360. [[CrossRef](#)]
16. Takahashi, J.; Takahashi, N.; Tadaishi, M.; Shimizu, M.; Kobayashi-Hattori, K. Valeric Acid Promotes Adipocyte Differentiation, Adiponectin Production, and Glucose Uptake via Its PPAR γ Ligand Activity. *ACS Omega* **2022**, *7*, 48113–48120. [[CrossRef](#)]
17. Sheu, M.-L.; Pan, L.-Y.; Hu, H.-Y.; Su, H.-L.; Sheehan, J.; Tsou, H.-K.; Pan, H.-C. Potential Therapeutic Effects of Thiazolidinedione on Malignant Glioma. *Int. J. Mol. Sci.* **2022**, *23*, 13510. [[CrossRef](#)]
18. Tsubouchia, Y.; Sano, H.; Kawahito, Y.; Mukaia, S.; Yamadaa, R.; Kohnoa, M.; Ichiroinouea, K.; Hla, T.; Kondoa, M. Inhibition of Human Lung Cancer Cell Growth by the Peroxisome Proliferator-Activated Receptor- γ Agonists through Induction of Apoptosis. *Biochem. Biophys. Res. Commun.* **2000**, *270*, 400–405. [[CrossRef](#)]
19. Khanna, S.; Sobhia, M.E.; Bharatam, P.V. Additivity of Molecular Fields: CoMFA Study on Dual Activators of PPAR α and PPAR γ . *J. Med. Chem.* **2005**, *48*, 3015–3025. [[CrossRef](#)]
20. Momose, Y.; Maekawa, T.; Yamano, T.; Kawada, M.; Odaka, H.; Ikeda, H.; Sohda, T. Novel 5-Substituted 2,4-Thiazolidinedione and 2,4-Oxazolidinedione Derivatives as Insulin Sensitizers with Antidiabetic Activities. *J. Med. Chem.* **2002**, *45*, 1518–1534. [[CrossRef](#)]
21. Kim, B.Y.; Ahn, J.B.; Lee, H.W.; Kang, S.K.; Lee, J.H.; Shin, J.S.; Kil Ahn, S.; Hong, C.I.; Yoon, S.S. Synthesis and biological activity of novel substituted pyridines and purines containing 2,4-thiazolidinedione. *Eur. J. Med. Chem.* **2004**, *39*, 433–447. [[CrossRef](#)] [[PubMed](#)]
22. Adams, A.D.; Yuen, W.; Hu, Z.; Santini, C.; Jones, A.; MacNaul, K.L.; Berger, J.P.; Doebber, T.W.; Moller, D.E. Amphipathic 3-Phenyl-7-propylbenzisoxazoles; human pPar γ , δ and α agonists. *Bioorg. Med. Chem. Lett.* **2003**, *13*, 931–935. [[CrossRef](#)] [[PubMed](#)]

23. Matos, L.H.S.; Masson, F.T.; Simeoni, L.A.; Homem-De-Mello, M. Biological activity of dihydropyrimidinone (DHPM) derivatives: A systematic review. *Eur. J. Med. Chem.* **2018**, *143*, 1779–1789. [[CrossRef](#)] [[PubMed](#)]
24. Lu, Y.; Guo, Z.; Guo, Y.; Feng, J.; Chu, F. Design, synthesis, and evaluation of 2-alkoxydihydrocinamates as PPAR agonists. *Bioorg. Med. Chem. Lett.* **2006**, *16*, 915–919. [[CrossRef](#)] [[PubMed](#)]
25. Kumar, R.; Ramachandran, U.; Srinivasan, K.; Ramarao, P.; Raichur, S.; Chakrabarti, R. Design, synthesis and evaluation of carbazole derivatives as PPAR α/γ dual agonists and antioxidants. *Bioorg. Med. Chem.* **2005**, *13*, 4279–4290. [[CrossRef](#)]
26. Kumar, R.; Mittal, A.; Ramachandran, U. Design and synthesis of 6-methyl-2-oxo-1,2,3,4-tetrahydro-pyrimidine-5-carboxylic acid derivatives as PPAR γ activators. *Bioorg. Med. Chem. Lett.* **2007**, *17*, 4613–4618. [[CrossRef](#)]
27. Bharathkumar, H.; Paricharak, S.; Dinesh, K.; Siveen, K.S.; Fuchs, J.E.; Rangappa, S.; Mohan, C.D.; Mohandas, N.; Kumar, A.P.; Sethi, G.; et al. Synthesis, biological evaluation and in silico and in vitro mode-of-action analysis of novel dihydropyrimidones targeting PPAR- γ . *RSC Adv.* **2014**, *4*, 45143–45146. [[CrossRef](#)]
28. Pascanu, V.; Miera, G.G.; Inge, A.K.; Martín-Matute, B. Metal–Organic Frameworks as Catalysts for Organic Synthesis: A Critical Perspective. *J. Am. Chem. Soc.* **2019**, *141*, 7223–7234. [[CrossRef](#)]
29. Holden, M.S.; Crouch, R.D. The Biginelli Reaction. *J. Chem. Educ.* **2001**, *78*, 1104. [[CrossRef](#)]
30. Alshorifi, F.T.; Ali, S.L.; Salama, R.S. Promotional Synergistic Effect of Cs–Au NPs on the Performance of Cs–Au/MgFe₂O₄ Catalysts in Catalysis 3,4-Dihydropyrimidin-2(1H)-Ones and Degradation of RhB Dye. *J. Inorg. Organomet. Polym. Mater.* **2022**, *32*, 3765–3776. [[CrossRef](#)]
31. Alshorifi, F.T.; Tobbala, D.E.; El-Bahy, S.M.; Nassan, M.A.; Salama, R.S. The role of phosphotungstic acid in enhancing the catalytic performance of UiO-66 (Zr) and its applications as an efficient solid acid catalyst for coumarins and dihydropyrimidinones synthesis. *Catal. Commun.* **2022**, *169*, 106479. [[CrossRef](#)]
32. Basappa, B.; Poonacha, L.K.; Zhang, X.; Vishwanath, D.; Yang, J.-R.; Nagaraja, O.; Swamynayaka, A.; Madegowda, M.; Chinnathambi, A.; Alharbi, S.A.; et al. Nano-zirconium dioxide catalyzed multi-component synthesis of bioactive pyranopyrazoles that targets cyclindependent kinase 1 in human breast cancer cells. *Biomedicines* **2023**, *11*, 172. [[CrossRef](#)] [[PubMed](#)]
33. Gadipelly, C.; Manneppalli, L.K. Nano-metal oxides for organic transformations. *Curr. Opin. Green Sustain. Chem.* **2019**, *15*, 20–26. [[CrossRef](#)]
34. Patil, R.V.; Chavan, J.U.; Dalal, D.S.; Shinde, V.S.; Beldar, A.G. Biginelli Reaction: Polymer Supported Catalytic Approaches. *ACS Comb. Sci.* **2019**, *21*, 105–148. [[CrossRef](#)] [[PubMed](#)]
35. Puripat, M.; Ramozzi, R.; Hatanaka, M.; Parasuk, W.; Parasuk, V.; Morokuma, K. The Biginelli Reaction Is a Urea-Catalyzed Organocatalytic Multicomponent Reaction. *J. Org. Chem.* **2015**, *80*, 6959–6967. [[CrossRef](#)]
36. Oliverio, M.; Costanzo, P.; Nardi, M.; Rivalta, I.; Procopio, A. Facile Ecofriendly Synthesis of Monastrol and Its Structural Isomers via Biginelli Reaction. *ACS Sustain. Chem. Eng.* **2014**, *2*, 1228–1233. [[CrossRef](#)]
37. Yao, B.-J.; Wu, W.-X.; Ding, L.-G.; Dong, Y.-B. Sulfonic Acid and Ionic Liquid Functionalized Covalent Organic Framework for Efficient Catalysis of the Biginelli Reaction. *J. Org. Chem.* **2021**, *86*, 3024–3032. [[CrossRef](#)]
38. Nevin, D.K.; Peters, M.B.; Carta, G.; Fayne, D.; Lloyd, D.G. Integrated Virtual Screening for the Identification of Novel and Selective Peroxisome Proliferator-Activated Receptor (PPAR) Scaffolds. *J. Med. Chem.* **2012**, *55*, 4978–4989. [[CrossRef](#)]
39. Liberato, M.V.; Nascimento, A.S.; Ayers, S.D.; Lin, J.Z.; Cvoró, A.; Silveira, R.L.; Martínez, L.; Souza, P.C.T.; Saidemberg, D.; Deng, T.; et al. Medium Chain Fatty Acids Are Selective Peroxisome Proliferator Activated Receptor (PPAR) γ Activators and Pan-PPAR Partial Agonists. *PLoS ONE* **2012**, *7*, e36297. [[CrossRef](#)]
40. Soler, J.M.; Artacho, E.; Gale, J.D.; García, A.; Junquera, J.; Ordejón, P.; Sánchez-Portal, D. The SIESTA method for ab initio order-*N* materials simulation. *J. Phys. Condens. Matter* **2002**, *14*, 2745–2779. [[CrossRef](#)]
41. Perdew, J.P.; Burke, K.; Ernzerhof, M. Generalized gradient approximation made simple. *Phys. Rev. Lett.* **1996**, *77*, 3865. [[CrossRef](#)]
42. Murugan, S.; Kavitha, C.V.; Purushothaman, A.; Nevin, K.G.; Sugahara, K.; Rangappa, K.S. A small Oxazine compound as an anti-tumor agent: A novel pyranoside mimetic that bind to VEGF, HB-EGF and TNF- α . *Cancer Lett.* **2010**, *297*, 231–243.
43. Bharathkumar, H.; Mohan, C.D.; Rangappa, S.; Kang, T.; Keerthy, H.K.; Fuchs, J.E.; Kwon, N.H.; Bender, A.; Kim, S.; Rangappa, K.S. Screening of quinoline, 1,3-benzoxazine, and 1,3-oxazine-based small molecules against iso-lated methionyl-tRNA synthetase and A549 and HCT116 cancer cells including an in silico binding mode analysis. *Org. Biomol. Chem.* **2015**, *13*, 9381–9387. [[CrossRef](#)] [[PubMed](#)]
44. Subramanian, G.; Babu Rajeev, C.P.; Mohan, C.D.; Sinha, A.; Chu, T.T.T.; Anusha, S.; Ximei, H.; Fuchs, J.E.; Bender, A.; Rangappa, K.S.; et al. Synthesis and in vitro evaluation of hydrazinyl phthalazines against malaria parasite, Plasmodium falciparum. *Bioorg. Med. Chem. Lett.* **2016**, *26*, 3300–3306. [[CrossRef](#)]
45. Fongmoon, D.; Shetty, A.K.; Basappa, Yamada, S.; Sugiura, M.; Kongtawelert, P.; Sugahara, K. Chondroitinase-mediated degradation of rare 3-O-sulfated glucuronic acid in functional oversulfated chondroitin sulfate K and E. *J. Biol. Chem.* **2007**, *282*, 36895–36904. [[CrossRef](#)] [[PubMed](#)]
46. Baburajeev, C.P.; Dhananjaya Mohan, C.; Ananda, H.; Rangappa, S.; Fuchs, J.E.; Jagadish, S.; Sivaraman Siveen, K.; Chinnathambi, A.; Ali Alharbi, S.; Zayed, M.E.; et al. Development of Novel Triazolo-Thiadiazoles from Heterogeneous "Green" Catalysis as Protein Tyrosine Phosphatase 1B Inhibitors. *Sci. Rep.* **2015**, *5*, 14195. [[CrossRef](#)] [[PubMed](#)]
47. Rangappa, K.S.; Basappa. New cholinesterase inhibitors: Synthesis and structure-activity relationship studies of 1,2-benzisoxazole series and novel imidazolyl-d 2-isoxazolines. *J. Phys. Org. Chem.* **2005**, *18*, 773–778. [[CrossRef](#)]

48. Basappa; Kavitha, C.V.; Rangappa, K.S. Simple and an efficient method for the synthesis of 1-[2-dimethylamino-1-(4-methoxyphenyl)-ethyl]-cyclohexanol hydrochloride: (+/-) venlafaxine racemic mixtures. *Bioorg. Med. Chem. Lett.* **2004**, *14*, 3279–3281. [[CrossRef](#)]
49. Sadashiva, M.P.; Basappa; Nanjunda Swamy, S.; Li, F.; Manu, K.A.; Sengottuvelan, M.; Prasanna, D.S.; Anilkumar, N.C.; Sethi, G.; Sugahara, K.; et al. Anti-cancer activity of novel dibenzo[b,f]azepine tethered isoxazoline derivatives. *BMC Chem. Biol.* **2012**, *12*, 5. [[CrossRef](#)] [[PubMed](#)]
50. Pandey, V.; Wang, B.; Mohan, C.D.; Raquib, A.R.; Rangappa, S.; Srinivasa, V.; Fuchs, J.E.; Girish, K.S.; Zhu, T.; Bender, A.; et al. Discovery of a small-molecule inhibitor of specific serine residue BAD phosphorylation. *Proc. Natl. Acad. Sci. USA* **2018**, *115*, E10505–E10514. [[CrossRef](#)]
51. Blanchard, V.; Chevalier, F.; Imberty, A.; Leeflang, B.R.; Basappa; Sugahara, K.; Kamerling, J.P. Conformational studies on five octasaccharides isolated from chondroitin sulfate using NMR spectroscopy and molecular modeling. *Biochemistry* **2007**, *46*, 1167–1175. [[CrossRef](#)] [[PubMed](#)]
52. Anusha, S.; Mohan, C.D.; Ananda, H.; Baburajeev, C.P.; Rangappa, S.; Mathai, J.; Fuchs, J.E.; Li, F.; Shanmugam, M.K.; Bender, A.; et al. Adamantyl-tethered-biphenylic compounds induce apoptosis in cancer cells by targeting Bcl homologs. *Bioorg. Med. Chem. Lett.* **2016**, *26*, 1056–1060. [[CrossRef](#)] [[PubMed](#)]
53. Basappa; Sugahara, K.; Thimmaiah, K.N.; Bid, H.K.; Houghton, P.J.; Rangappa, K.S. Anti-tumor activity of a novel HS-mimetic-vascular endothelial growth factor binding small molecule. *PLoS ONE* **2012**, *7*, e39444. [[CrossRef](#)]
54. Sebastian, A.; Pandey, V.; Mohan, C.D.; Chia, Y.T.; Rangappa, S.; Mathai, J.; Baburajeev, C.P.; Paricharak, S.; Mervin, L.H.; Bulusu, K.C.; et al. Novel Adamantanyl-Based Thiadiazolyl Pyrazoles Targeting EGFR in Triple-Negative Breast Cancer. *ACS Omega*. **2016**, *1*, 1412–1424. [[CrossRef](#)] [[PubMed](#)]
55. Rakesh, K.S.; Jagadish, S.; Vinayaka, A.C.; Hemshekhar, M.; Paul, M.; Thushara, R.M.; Sundaram, M.S.; Swaroop, T.R.; Mohan, C.D.; Basappa; et al. A new ibuprofen derivative inhibits platelet aggregation and ROS mediated platelet apoptosis. *PLoS ONE* **2014**, *9*, e107182. [[CrossRef](#)] [[PubMed](#)]
56. Kumar, C.A.; Jayarama, S.; Basappa; Salimath, B.P.; Rangappa, K.S. Pro-apoptotic activity of imidazole derivatives mediated by up-regulation of Bax and activation of CAD in Ehrlich Ascites Tumor cells. *Investig. New Drugs* **2007**, *25*, 343–350. [[CrossRef](#)]
57. Basappa; Rangappa, K.S.; Sugahara, K. Roles of glycosaminoglycans and glycanmimetics in tumor progression and metastasis. *Glycoconj. J.* **2014**, *31*, 461–467. [[CrossRef](#)]
58. Sunitha, K.; Hemshekhar, M.; Gaonkar, S.L.; Sebastin Santhosh, M.; Suresh Kumar, M.; Basappa; Priya, B.S.; Kemparaju, K.; Rangappa, K.S.; Nanjunda Swamy, S.; et al. Neutralization of haemorrhagic activity of viper venoms by 1-(3-dimethylaminopropyl)-1-(4-fluorophenyl)-3-oxo-1,3-dihydroisobenzofuran-5-carbonitrile. *Basic Clin. Pharm. Toxicol.* **2011**, *109*, 292–299. [[CrossRef](#)]
59. Jagadish, S.; Rajeev, N.; Naveen Kumar, S.K.; Sharath Kumar, K.S.; Paul, M.; Hegde, M.; Basappa; Sadashiva, M.P.; Girish, K.S.; Rangappa, K.S. Platelet protective efficacy of 3,4,5 trisubstituted isoxazole analogue by inhibiting ROS-mediated apoptosis and platelet aggregation. *Mol Cell Biochem.* **2016**, *414*, 137–151. [[CrossRef](#)]
60. Bharathkumar, H.; Sundaram, M.S.; Jagadish, S.; Paricharak, S.; Hemshekhar, M.; Mason, D.; Kemparaju, K.; Girish, K.S.; Basappa; Bender, A.; et al. Novel benzoxazine-based aglycones block glucose uptake in vivo by inhibiting glycosidases. *PLoS ONE* **2014**, *9*, e102759. [[CrossRef](#)]
61. Priya, B.S.; Anil Kumar, C.; Nanjunda Swamy, S.; Basappa; Naveen, S.; Shashidhara Prasad, J.; Rangappa, K.S. 2-(2-(2-Ethoxybenzoylamino)-4-chlorophenoxy)-N-(2-ethoxybenzoyl)benzamine inhibits EAT cell induced angiogenesis by down regulation of VEGF secretion. *Bioorg. Med. Chem. Lett.* **2007**, *17*, 2775–2780. [[CrossRef](#)] [[PubMed](#)]
62. Kwon, N.H.; Lee, J.Y.; Ryu, Y.L.; Kim, C.; Kong, J.; Oh, S.; Kang, B.S.; Ahn, H.W.; Ahn, S.G.; Jeong, J.; et al. Stabilization of Cyclin-Dependent Kinase 4 by Methionyl-tRNA Synthetase in p16INK4a-Negative Cancer. *ACS Pharm. Transl. Sci.* **2018**, *1*, 21–31. [[CrossRef](#)] [[PubMed](#)]
63. Morris, G.M.; Huey, R.; Lindstrom, W.; Sanner, M.F.; Belew, R.K.; Goodsell, D.S.; Olson, A.J. AutoDock4 and AutoDockTools4: Automated docking with selective receptor flexibility. *J. Comput. Chem.* **2009**, *30*, 2785–2791. [[CrossRef](#)] [[PubMed](#)]
64. Schrödinger, L.L.C. *Schrödinger Release 2020-1: Maestro*; Schrödinger, LLC: New York, NY, USA, 2020.
65. Wallace, A.C.; Laskowski, R.A.; Thornton, J.M. LIGPLOT: A program to generate schematic diagrams of protein-ligand interactions. *Protein Eng.* **1995**, *8*, 127–134. [[CrossRef](#)]

Disclaimer/Publisher's Note: The statements, opinions and data contained in all publications are solely those of the individual author(s) and contributor(s) and not of MDPI and/or the editor(s). MDPI and/or the editor(s) disclaim responsibility for any injury to people or property resulting from any ideas, methods, instructions or products referred to in the content.